Structural mechanism of biased activation of T cell receptor by a high-affinity antibody

Xiang Li[1#], Buliao Huang[1#], Enze Shao[1#], Yuwei Zhu[1#], Dehui Yang[1], Yan Chen[1], Wenbo Gao[1], Zebin Lu[1], Fengliang Lu[2], Anqi Zhang[1], Changyou Guo[1], Zhiwei Huang[*1,3,4]

Antibodies targeting the TCR–CD3 complex are widely used in cancer therapy but limited by cytokine release syndrome (CRS). Here we identified a TCR–CD3-specific antibody, 4B1, with high binding affinity. Compared to the well-known anti-TCR–CD3 antibody OKT3, 4B1 leads to enhanced T cell activation but significantly reduced cytokine release. 4B1-based bispecific antibodies (BsAbs) demonstrate superior tumor elimination capability with lower cytokine-inducing activity in humanized mice, suggesting that 4B1 uncouples T cell cytotoxicity from inflammatory cytokine release. Cryo-EM analysis reveals that 4B1 Fab binds specifically to a single CD3ε subunit, forming a 1:1 stoichiometry with the TCR–CD3 complex, while OKT3 Fab binds to both CD3ε subunits, resulting in a 2:1 stoichiometry. Confocal microscopy reveals that 4B1 induces mild TCR clustering, while OKT3 leads to robust clustering of TCR–CD3 complexes. In addition, 4B1 triggers delayed and milder CD3ζ phosphorylation and intracellular calcium signals in T cells compared to rapid, potent responses triggered by OKT3. Collectively, these data indicate that CRS depends on the extent of TCR clustering induced by TCR–CD3 antibodies rather than on their binding affinity. Our study identifies a novel TCR–CD3-specific antibody and reveals its biased mechanism for T cell activation, opening new opportunities for safer and more effective TCR-targeting therapeutics.

https://doi.org/10.15302/vita.2026.03.0021

INTRODUCTION

The T cell receptor (TCR) complex consists of a TCRα/β module, which is responsible for recognizing antigens, and three dimeric CD3 modules (CD3γ/ε, CD3δ/ε', CD3ζ/ζ'), which play a crucial role in initiating intracellular signaling[1-3]. Each TCR–CD3 complex incorporates two ε chains that pair with both γ and δ chains to form CD3γ/ε and CD3δ/ε', respectively. Among these, CD3ε acts as a chaperone during the assembly and folding of all other CD3 subunit proteins, making it pivotal in T cell activation[4,5]. T cell triggering is initiated by the interaction between agonistic peptide-major histocompatibility complex (pMHC) or ligand and the extracellular domains of the TCR. This interaction induces conformational changes in the plasma membrane and cytoplasmic domains of the TCR–CD3 complex[6,7]. As a result, the cytoplasmic tails of CD3ε and CD3ζ become exposed, facilitating the phosphorylation of the immunoreceptor tyrosine-based activation motif (ITAM) tails of both CD3ζ and CD3ε[8,9]. ITAM phosphorylation triggers a cascade of downstream signaling events that ultimately lead to the release of cytotoxic perforins, granzymes, and cytokines, thus inducing apoptosis in target cells[10-12].

Targeting the TCR–CD3 complex can activate T cells in a manner independent of MHC restriction[13]. Upon binding to the TCR–CD3 complex, anti-CD3 monoclonal antibodies cross-link TCRs, thereby inducing the formation of TCR microclusters. The extent of TCR clustering is significantly and positively correlated with the magnitude of T cell activation[14]. Greater TCR clustering accelerates the phosphorylation of ITAMs on the CD3ζ chains, thereby potentiating downstream signaling pathways — including calcium mobilization, and the activation of NFAT and NF-κB — ultimately driving the transcriptional upregulation of cytokine-coding genes (such as TNF-α, IFN-γ, and IL-6), and enhancing cytokine secretion[15,16]. CD3-targeting monoclonal antibodies, as well as bispecific T cell engagers, have been widely developed in research and clinical fields[17]. A well-known example is the anti-CD3 monoclonal antibody OKT3, which is widely used for the *ex vivo* activation and expansion of primary T cells, CAR-T cells, and TCR-T cells in adoptive cell therapies[5,18]. In addition to cancer immunotherapy, anti-CD3 antibodies have also been employed to induce immune tolerance. The tolerogenic effect of anti-CD3 antibodies is induced through the initiation of a strong TCR–CD3 signal in the absence of co-stimulation signals, which ultimately leads to T cell anergy or apoptosis[19-21]. While repetitive administration of OKT3 effectively suppresses the immune rejection after renal transplantation, it also triggers the cytokine release syndrome (CRS)[22-24], characterized by T cell activation and the release of inflammatory cytokines, followed by a state of anergy or apoptosis. Recently, Teplizumab, a CD3 binding affinity-modified variant of OKT3 that reduces inflammatory cytokine release, has received FDA approval for its use in delaying the onset of type 1 diabetes[25,26].

T cell engaging bispecific antibodies (T-BsAbs) combine two antibodies with one being specific for CD3 and the other for a tumor-associated antigen (TAA). These artificially engineered

1. HIT Center for Life Sciences, School of Life Science and Technology, Harbin Institute of Technology, Harbin, Heilongjiang, China. 2. Harbin Blood Center, Harbin, Heilongjiang, China. 3. Westlake Center for Genome Editing, Westlake Laboratory of Life Sciences and Biomedicine, School of Life Sciences, Westlake University, Hangzhou, Zhejiang, China. 4. New Cornerstone Science Institute, Harbin Institute of Technology, Harbin, Heilongjiang, China. #These authors contributed equally to this work. *Correspondence: Zhiwei Huang (huangzhiwei@hit.edu.cn)

Received: October 26, 2025; Accepted: March 12, 2026; Published: June 2, 2026

bispecific monoclonal antibodies simultaneously bind to T cells and tumor cells, triggering T cell activation. This activation induces the release of granzymes and perforins into the immunological synapse, ultimately leading to the elimination of malignant cancer cells[27-29]. Blinatumomab is a CD3-targeting T-BsAb that has been FDA-approved for the treatment of acute lymphoblastic leukemia[28,30]. The CD3-targeting arm of Blinatumomab is derived from the OKT3 antibody, which has a reduced CD3 binding affinity to minimize the incidence of CRS[31-33].

CRS is also the primary adverse event associated with T-BsAbs and CAR-T cell therapies[34]. The high binding affinity between CD3 and a CD3-targeting antibody correlates positively with the potency of T-BsAbs but also leads to increased cytokine production and a higher risk of CRS[35-37]. Therefore, recent efforts have focused on developing antibodies with reduced affinity for TCR–CD3, aiming to uncouple T cell killing from inflammatory cytokine secretion[35,38-40]. However, lowering the binding affinity for CD3 to mitigate CRS compromises the tumor-killing effect[40].

Currently, the mechanism by which TCR–CD3 recognition by its antibodies contributes to T cell activation and cytokine release remains unknown. In this study, an antibody named 4B1 was identified to possess pico-molar (pM) binding affinity with TCR–CD3. Compared to OKT3, 4B1 exhibits stronger potency in T cell activation while inducing less inflammatory cytokine release. The cryo-electron microscopy (cryo-EM) structures revealed that 4B1 Fab binds exclusively to the ε subunit of CD3γ/ε, in contrast to OKT3 Fab, which interacts with both ε subunits of TCR–CD3. In humanized mouse models, 4B1-based BsAbs showed higher tumor cell killing ability but significantly lower cytokine release than OKT3-BsAbs. Together, our study identifies a highly specific CD3 antibody that can induce biased T cell activation. These findings not only suggest a mechanism elucidating CRS but also open new avenues for the development of next-generation T cell activation antibodies.

RESULTS

The higher-affinity anti-CD3 antibody 4B1 reduces cytokine release compared to OKT3

To investigate the mechanism of TCR activation by TCR–CD3-targeting antibodies, we generate a number of monoclonal antibodies targeting the TCR–CD3 complex. One of these, named 4B1, was selected for characterizing due to its high binding affinity to the TCR–CD3 complex. We compared 4B1 by benchmarking it against two reference antibodies: UCHT1 and OKT3. UCHT1 is a well-characterized mouse monoclonal antibody that recognizes the CD3ε subunit of the human TCR–CD3 complex with exceptionally high (pico-molar) affinity; it is widely used in immunology research as a potent T cell activator and for immunoprecipitation of the TCR–CD3 complex. Structural studies have shown that it can engage CD3ε in both the CD3γε and CD3δε heterodimers[41]. OKT3, in contrast, is the most widely used clinical and experimental benchmark, binding TCR–CD3 complex with lower affinity than 4B1 (Fig. 1a) [42]. Subsequent *in vitro* human $CD3^+$ T cell activation experiments using these antibodies revealed that both 4B1 and UCHT1 triggered comparable levels of CD69, an early marker of T cell activation. The CD69-inducing activity of 4B1 was higher than that of OKT3 (Fig. 1b; Supplementary Table S1). Following 48 h of activation, 4B1- and OKT3-stimulated cells showed similar levels of perforin and granzyme B, while UCHT1 induced slightly higher levels of both molecules

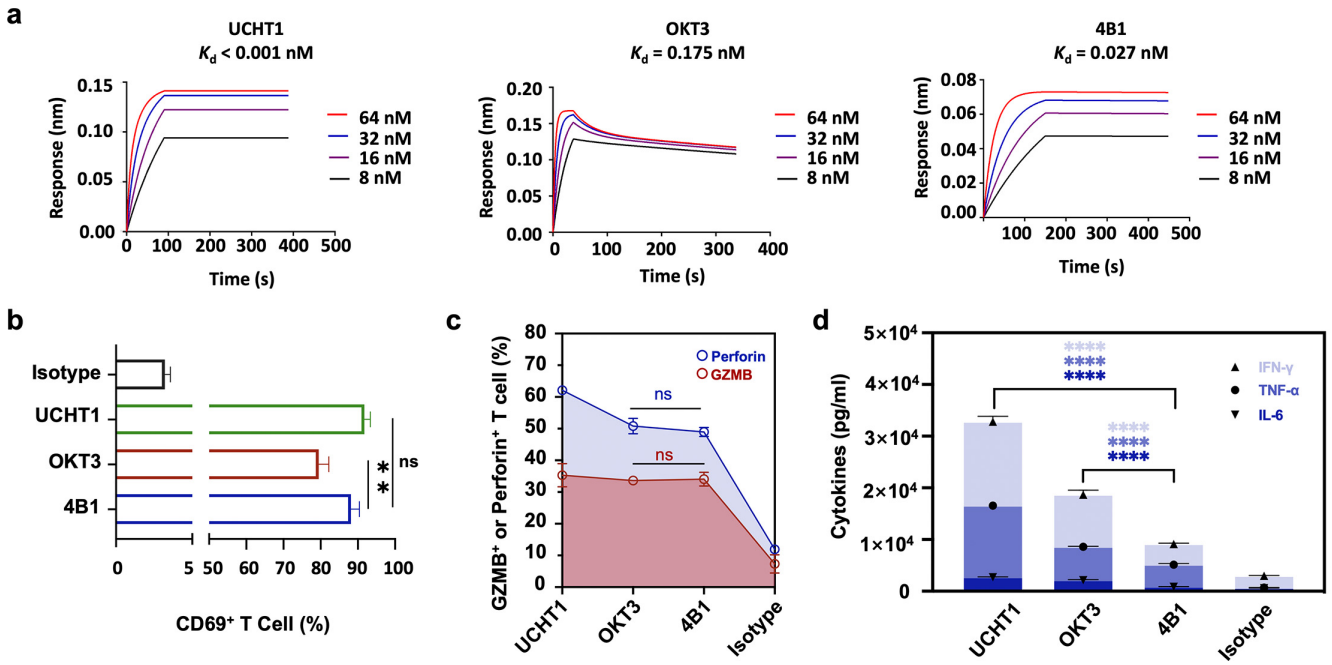

Fig. 1 Identification of a novel TCR–CD3-targeting antibody with high binding affinity and low cytokine release. a Binding affinities of native TCR–CD3 protein complex with activation antibodies OKT3, 4B1 and UCHT1 targeting CD3ε, measured by bio-layer interferometry. Colored curves are the experimental traces obtained from bio-layer interferometry experiments, and the data were used to calculate the equilibrium-dissociation constant (K_d) values. Data are representative of three independent experiments. **b** 10 nM of various antibodies were used to stimulate human T cells. Percentages of $CD69^+$ T cells were measured at the 24 h time point. Data are presented as mean ± SEM, $n = 3$. Statistical significance was calculated with one-way ANOVA: $^{**}P < 0.01$. **c** T cells were incubated with 10 nM monoclonal antibodies for 48 h， anti-human IgG was used as an isotype control. Percentages of $GZMB^+$ or $perforin^+$ cells were measured. Data are presented as mean ± SEM, $n = 3$. Statistical significance was calculated with one-way ANOVA. ns, not significant. **d** Measurement of cytokine release (IFNγ, TNF-α and IL-6) after human $CD3^+$ T cells were cultured under the conditions described in **c**. Data are presented as mean ± SEM, $n = 3$. Statistical significance was calculated with one-way ANOVA. OKT3 vs 4B1: $^{****}P < 0.0001$.

among the tested antibodies (Fig. 1c). Consistent with previous data[43], UCHT1 induced higher levels of inflammatory cytokines than OKT3 (Fig. 1d). This agrees with the idea that a TCR activation antibody with higher affinity typically associates with higher cytokine release activity[44,45]. However, unexpectedly, 4B1 displayed much lower activity in inducing the release of inflammatory cytokines compared to UCHT1 and OKT3.

4B1 BsAbs efficiently kill tumor cells but exhibit limited cytokine-inducing activity

Next, we investigated the tumor cell killing effects mediated by the 4B1 BsAbs. We generated two formats of 4B1 BsAbs: IgG-scFv (4B1/anti-TAA)[46] (Fig. 2a) and CrossMab (4B1×anti-TAA)[47] (Fig. 3a). Both antibodies contained Fc silencing mutations, with Leu234 and Leu235 replaced with alanine, and Pro329 replaced with glycine[48]. For *in vitro* assay, the carcinoembryonic antigen (CEA)-targeting antibody was fused to 4B 1 and OKT3 to create 4B1/anti-CEA and OKT3/anti-CEA BsAbs, respectively. $CD3^+$ T cells were pre-incubated with the BsAbs for 25 min, followed by washing steps (Fig. 2b). The culture was then incubated with the CEA-expressing MKN45 human gastric cancer cells for 48 h. Subsequently, the levels of cytokines (IL-2, IL-6, IL-10, IFN-γ, and TNF-α) and tumor cell lysis were measured. Both 4B1/anti-CEA and OKT3/anti-CEA induced potent T cell-mediated killing of CEA-positive MKN45 cells in a dose- and antigen-dependent manner, achieving similar maximum levels of tumor cell killing. In contrast, the HeLa cell line, which lacks CEA expression, was resistant to lysis (Fig. 2c). Strikingly, at a saturating killing dose of ~50 nM, 4B1/anti-CEA stimulated significantly less cytokine release compared to OKT3/anti-CEA. Specifically, OKT3/anti-CEA triggered the release of > 300,000 pg/mL of IFN-γ and 20,000 pg/mL of TNF-α, whereas 4B1/anti-CEA stimulated the release of approximatel 10,000 pg/mL of IFN-γ and less than 5,000 pg/mL of TNF-α (Fig. 2c). These findings highlight the potent tumor-killing activity of 4B1/anti-CEA while demonstrating its reduced cytokine-inducing activity, which may be beneficial in minimizing cytokine-related side effects.

To further assess the functional robustness of 4B1 BsAbs under low antigen expression conditions, we evaluated their efficacy against tumor cells expressing low levels of tumor-associated antigen. The LOVO human colon adenocarcinoma cell line was selected, as it displays significantly lower surface expression of CEA compared to MKN45 cells (Supplementary Fig. S1a). In co-culture assays with human T cells, both 4B1/anti-CEA and OKT3/anti-CEA mediated potent, dose-dependent cytotoxicity against LOVO cells (Supplementary Fig. S1b). Notably, even under low antigen density, 4B1/anti-CEA induced substantially lower release of inflammatory cytokines such as IFN-γ and TNF-α compared to OKT3/anti-CEA (Supplementary Fig. S1c). These results demonstrate that 4B1 maintains efficient tumor cell killing while preserving a low cytokine release profile, even when target cells exhibit low antigen expression.

To investigate whether the observed differences in cytokine release profiles between OKT3 and 4B1 bispecific molecules are present in other tumor cells expressing different antigens, we conjugated 4B1 and OKT3 with an anti-CD19 arm, respectively, and performed a primary T cell killing assay using the Raji cell line. Supporting the data from the CEA-positive MKN45 cells, OKT3/anti-CD19 enhanced the maximal induction of cytokine release, stimulating the release of over 40,000 pg/mL of IL-2 and IFN-γ. In contrast, 4B1/anti-CD19 triggered the release of approximately 10,000 pg/mL of IL-2 and 15,000 pg/mL of IFN-γ at the maximum killing dose of 100 nM. The EC50 values for both bispecific antibodies were similar (Fig. 2d). *In vitro* potency against tumor cells by 4B1 BsAb was further assessed using peripheral blood mononuclear cells (PBMCs) obtained from nine healthy human donors (Supplementary Fig. S2a). Following 48 h of incubation, comparable maximal killing levels were observed for 4B1/anti-CEA and OKT3/anti-CEA (Supplementary Fig. S2b). However, the releases of IFN-γ and TNF-α cytokines induced by 4B1/anti-CEA were significantly lower than those induced by OKT3/anti-CEA across all nine donors (Supplementary Fig. S2c). Collectively, these results indicate that 4B1-containing BsAbs induce less cytokine release than OKT3-containing BsAbs in PBMC from different donors.

4B1 BsAbs mediate more potent tumor cell-killing but induce lower cytokine release than OKT3 BsAbs in humanized mice

To evaluate the *in vivo* tumor cell-killing and cytokine release profiles of 4B1 BsAb, we utilized a Raji lymph blastoma xenograft mouse model to compare the functional effects of 4B1×anti-CD19 and OKT3×anti-CD19[49] (Fig. 3a).

Human $CD19^+$ Raji cells stably expressing luciferase were engrafted into NKG mice for 7 days, followed by intravenous injection of pre-incubated human PBMCs with titrated concentrations of BsAbs (Fig. 3b). Mice treated with isotype control, OKT3 mAb or 4B1 mAb showed tumor progression in the absence of BsAb engagement. The data showed that both the OKT3×anti-CD19 and the 4B1×anti-CD19 groups achieved strong tumor cell killing effects at multiple dose levels. Notably, at Day 22, the 4B1×anti-CD19 group showed nearly complete tumor clearance at 10 μg, with the tumor fluorescence intensity detected being significantly lower than that in the OKT3×anti-CD19 group at the 10 μg dose ($P < 0.01$) (Fig. 3c). Consistently, all mice in the control and vehicle groups died within 25 days after tumor seeding, whereas all mice receiving treatment with 4B1×anti-CD19 and OKT3×anti-CD19 BsAbs survived beyond 30 days (Fig. 3d).

Clinical studies on BsAb immunotherapy have indicated that cytokine storm occurs following the initial administration[24]. In order to investigate the cytokine release triggered by 4B1 BsAb in mice, peripheral blood serum samples were collected at various time points subsequent to the first BsAb treatment. Treatment with OKT3×anti-CD19 resulted in the release of substantial levels of systemic proinflammatory cytokines, including IL-2, IFN-γ, IL-10, TNF-α, and IL-6, peaking at 2 h after the initial dose administration. Remarkably, treatment with 4B1×anti-CD19 triggered significantly lower cytokine release of IL-2, IL-10, IFN-γ, and TNF-α compared to OKT3×anti-CD19 (Fig. 3e). Thus, in terms of both the peak and duration of cytokine release, 4B1×anti-CD19 leads to a reduced response than OKT3×anti-CD19.

4B1 Fab and OKT3 Fab interact with the single and dual epitopes on TCR–CD3 complex, respectively

To investigate the structural mechanisms underlying the significant reduction in cytokine release triggered by 4B1 mAb compared to OKT3 mAb, we performed cryo-EM analyses of TCR–CD3 in complex with 4B1 and OKT3. Firstly, we expressed and purified the TCR–CD3 complex and 4B1 protein in 293F cells. Subsequently, the TCR–CD3 complex protein

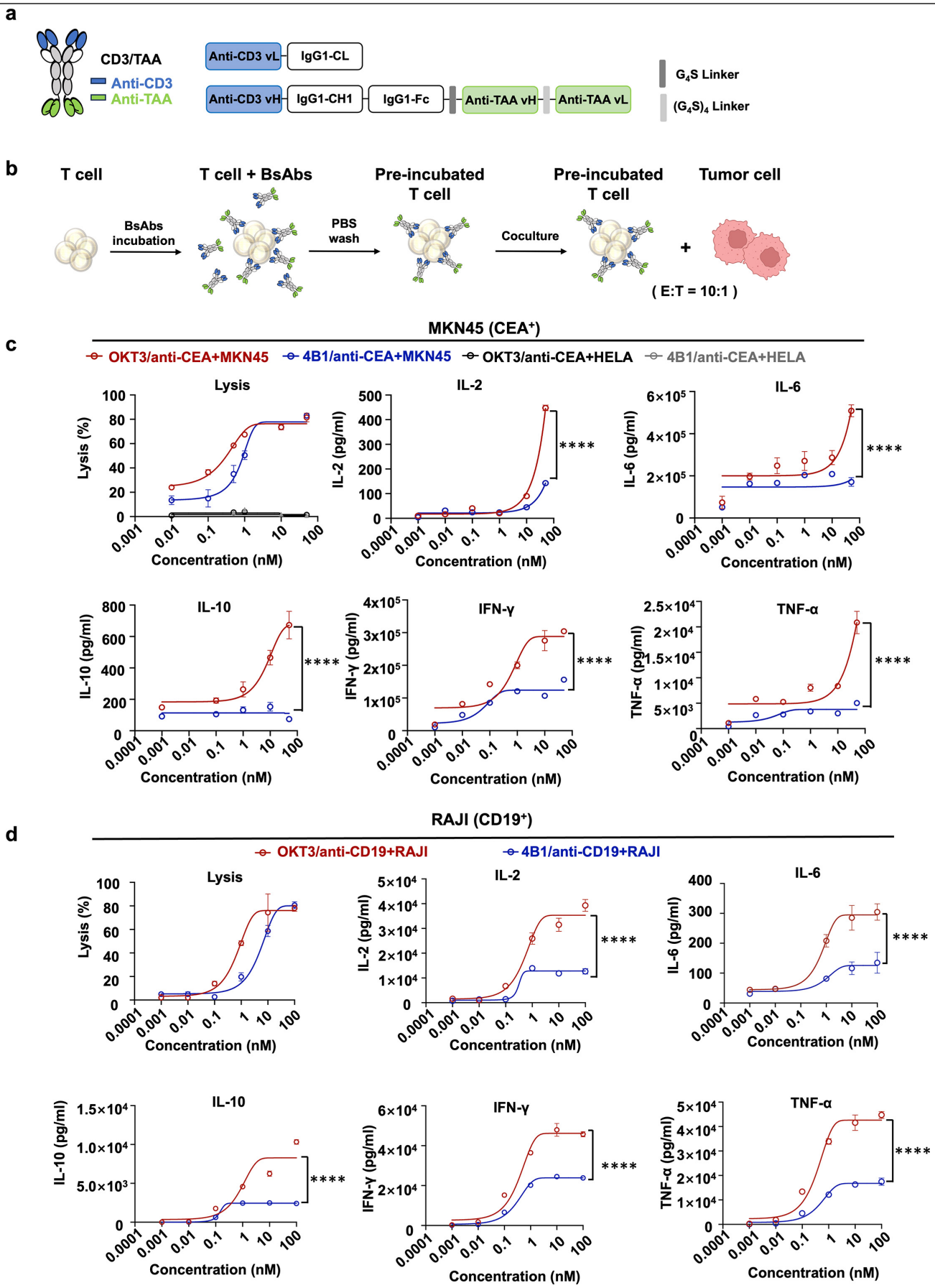

Fig. 2 4B1 BsAbs efficiently kill tumor cells with limited cytokine release. a Schematic diagram of BsAb in the anti-CD3/anti-TAA format. **b** 1×10^7 /mL human T cells were incubated with increasing concentrations of anti-CD3/anti-TAA-BsAb for 30 min (pre-incubated), washing with 1× PBS buffer (twice). The pre-incubated T cells were then co-cultured with target cells at an E:T ratio of 10:1 at 37 °C for 24 h (Raji) or 48 h (MKN45). Hela cells were used as a negative control. **c**, **d** Measurements of IL-2, IL-6, IL-10, IFN-γ, and TNF-α secretions in the supernatants from the co-culture conditions described in **b**. Cytokine levels in the media were analyzed by Biolegend Human Cytokine Assay. Data are presented as mean ± SEM, *n* = 3. Statistical significance was calculated with two-way ANOVA: ****$P < 0.0001$.

was mixed with the Fab region of 4B1 antibody, and the 4B1–TCR–CD3 complex was co-purified through gel filtration. The eluted 4B1–TCR–CD3 protein complex was concentrated and subsequently prepared on a grid for cryo-EM analysis. After multiple rounds of 2D and 3D classification, a subset of 439,348 particles were used for image reconstruction, yielding a map with a global resolution of 3.14 Å, based on the gold-standard Fourier shell correlation (Supplementary Fig. S3a–d). The well-resolved cryo-EM map allows for the precise assignment of the residues mediating 4B1 Fab interaction with the TCR–CD3 complex. As shown in Fig. 4a, the 4B1 Fab molecule forms a 1:1 stoichiometric complex with the TCR–CD3 complex. The 4B1 Fab molecule packs against the CD3δε heterodimer through making direct interactions with the extracellular domain (ECD) of CD3ε subunit (Fig. 4a). The buried surface area at the interface is approximately 871 $Å^2$, to which the 4B1 light and heavy chains contribute 354.3 $Å^2$ and 516.7 $Å^2$, respectively.

To compare the recognition mechanisms between 4B1 Fab and OKT3 Fab in relation to the TCR–CD3 complex, we determined the cryo-EM structure of the TCR–CD3 complex bound to OKT3 Fab at a resolution of 3.18 Å (Supplementary Fig. S4a–d). The well-resolved cryo-EM map indicates that OKT3 Fab interacts with the TCR–CD3 complex in a stoichiometry of 2:1, compared to the 1:1 interaction between 4B1 Fab and TCR–CD3. Two molecules of OKT3 Fab interact with the CD3δ/ε and CD3γ/ε heterodimers of the TCR–CD3 complex, respectively (Fig. 4b). Interestingly, the structural alignment of 4B1–TCR–CD3 and OKT3–TCR–CD3 reveals that 4B1 Fab and OKT3 Fab recognize overlapping epitopes on the CD3ε subunit of CD3δ/ε. However, there is a notable difference in their interaction with CD3ε. The 4B1 Fab rotates approximately 45° relative to the OKT3 Fab in order to interact with CD3ε (Fig. 4c). Docking of the 4B1 Fab onto the CD3ε subunit of CD3γ/ε reveals a severe steric clash with the TCRβ subunit (Fig. 4d). These structural observations provide the mechanism for the observed 1:1 stoichiometry between the 4B1 Fab and the TCR–CD3 complex. We then used flow cytometry to assay the binding efficiency of the 4B1 and OKT3 antibodies for human T cells. Further supporting the structural observations, the results from the assay indicated that both antibodies demonstrated efficient TCR–CD3 binding (Fig. 4e). However, analysis of the mean fluorescence intensity (MFI) revealed that OKT3 exhibited approximately twice the binding capacity of 4B1. Additionally, the EC50 values of these two antibodies were found to be similar. To verify whether this spatial constraint might be altered in T cells that naturally lack the canonical TCRβ chain or possess a different local architecture, such as γδ T cells. Binding assays using the 4B1 and OKT3 monoclonal antibodies were performed on human γδ T cells. 4B1 and OKT3 exhibited comparable binding signals (MFI) on γδ T cells (Supplementary Fig. S5a). This result stands in sharp contrast to the outcome observed in αβ T cells, where 4B1 exhibited only half the binding signal of OKT3 (Fig. 4e), which aligns with the different stoichiometries observed in the Fab–TCR complex structures. Together, these data further support that steric constraint is a primary determinant of the biased signaling mediated by 4B1.

Specific recognition of the TCR–CD3 complex by 4B1

In the cryo-EM structure of 4B1–TCR–CD3, the interface between the 4B1 complementarity-determining regions (CDRs) and the CD3ε ECD involves a network of hydrogen bonds and salt bridge interactions (Fig. 5a). Specifically, residues Y52 of CDR loop 1 of the light chain (CDRL1), Y70 of CDRL2, and H112 of CDRL3 interact with residues Q60, N65, and E106 of CD3ε through three hydrogen bonds (Fig. 5b). On the heavy chain of 4B1, residues R50, Y119, R120, Y121, D122, and Y124 of CDRH1 and CDRH3 form hydrogen bonds and salt bridge interactions with CD3ε residues E70, E56, D78, R101, and G102, respectively. Additionally, residue E69 from the CDRH framework region establishes a salt bridge with R101 of CD3ε, thereby reinforcing the interactions (Fig. 5c). Consistent with our structural observation, mutations in the residues involved in the binding between 4B1 and CD3ε significantly impaired the interactions between 4B1 and TCR–CD3, as well as the activation of T cells (Fig. 5d, e). The original representative SDS-PAGE gels for these binding assays are provided in Supplementary Fig. S6a, b. 4B1 and OKT3 both bind to the E56, R101 epitopes on CD3, while mutations at Q60, E70, and E106 residues reduced 4B1 binding to TCR–CD3 but did not affect OKT3 binding (Fig. 5f). Taken together, the structural comparison between 4B1–TCR–CD3 and OKT3–TCR–CD3, in combination with biochemical data, supports the conclusion that 4B1 and OKT3 bind to overlapping but distinct epitopes on the TCR–CD3 complex.

The lower avidity of 4B1 results in milder and delayed T cell activation signaling compared to OKT3

The potency of a T-cell activating antibody is primarily determined by the strength of its initial signal, assessed via the degree of TCR clustering[50,51]. To check whether high avidity OKT3 induces more potent TCR clustering than 4B1 on the membrane, immunofluorescence staining of T cells was performed following stimulation with these antibodies. Confocal microscopy revealed that OKT3 strongly cross-links TCRs, leading to robust clustering of TCR complexes and the formation of large immune synapses (Fig. 6a, b). In contrast, 4B 1 induces mild TCR clustering.

To investigate the intracellular mechanisms underlying the different T cell activation phenotypes of 4B1 and OKT3, we first examined CD3ζ phosphorylation triggered by these antibodies in human T cells. Our data showed that OKT3 induces rapid and significantly increased CD3ζ phosphorylation at various concentrations, whereas 4B1 induces slower and milder CD3ζ phosphorylation (Fig. 6c, d). We also evaluated the phosphorylation of ERK, a key kinase regulating downstream gene expression. It is well established that ERK phosphorylation levels are correlated with downstream cytokine expression[52,53]. Consistently, OKT3 triggered more potent and earlier ERK phosphorylation than 4B1 at various time points (Fig. 6c, d). ERK phosphorylation peaked within 1 min, reaching four times the level of that triggered by 4B1 at the same time point. As a crucial second messenger, intracellular calcium mobilization is essential for translating TCR engagement into downstream functional responses. Since calcium-dependent pathways are intrinsically involved in T cell activation[54], we next examined intracellular calcium signals in T cells at different concentrations of OKT3 and 4B1 over time. Strikingly, 4B1 induced a delayed and more moderate calcium release compared to OKT3 (Fig. 6e). In summary, 4B1 and OKT3 induce different degrees of activation of intracellular signaling pathways. 4B1, by binding to a single epitope on the TCR–CD3 complex, triggers finely tuned intracellular signaling cascades compared to OKT3 for T cell activation.

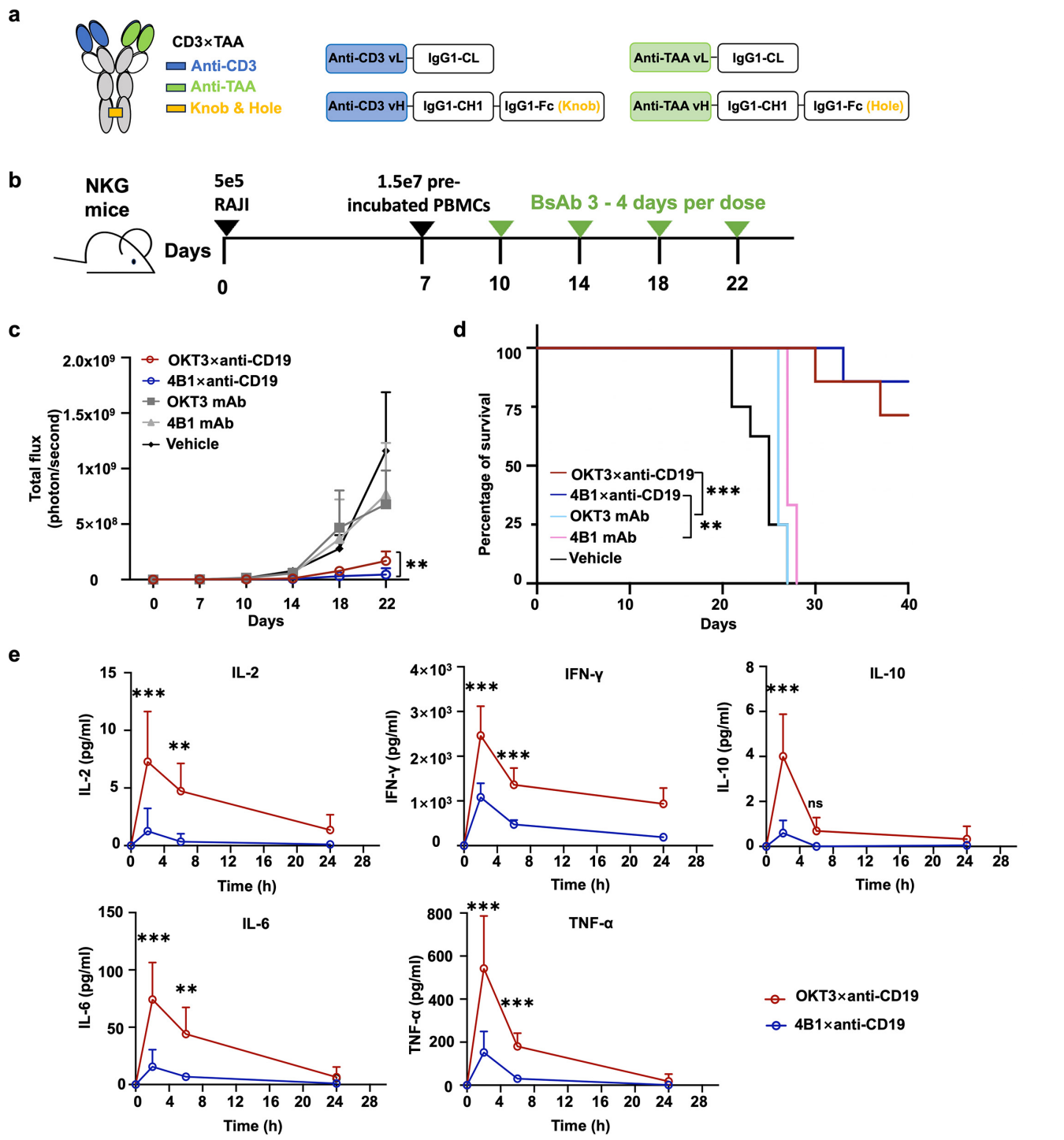

Fig. 3 4B1 BsAb achieves a more efficient Raji cell-killing effect and triggers a significant lower cytokine release than OKT3 BsAb in humanized mice. a Schematic diagram of BsAb in the anti-CD3×anti-TAA format. **b** NKG mice engrafted with 5 × 10^5 luciferase-labeled Raji tumor cells at day 0, 1.5 × 10^7 pre-incubated PBMCs were injected 7 days later. 10 μg BsAbs and mAbs were administered twice weekly for three weeks per mouse. Tumor burden was assessed before each antibody dose using bioluminescent imaging from days 7 to 22. The numbers indicated in **b** represent the days post-tumor implantation. **c** Quantitation of bioluminescence of Luc^+ tumors post-treatment (OKT3×anti-CD19, 4B1×anti-CD19 and vehicle, n = 7; OKT3 mAb, n = 4 and 4B1 mAb, n = 3). Statistical significance was reported at day 22, calculated with multiple unpaired t-test: $^{**}P < 0.01$. **d** Kaplan-Meier survival curve of mice in **c** (n = 3–7). Statistical significance was calculated with log-rank test: $^{**}P < 0.01$, $^{***}P < 0.001$. **e** After intravenous injection of pre-incubated T cells and PBMCs into Raji-bearing mice, serum cytokine levels were measured at different time points (2, 6, 24 h after injection). Data are presented as mean ± SEM, n = 7. Statistical significance was calculated with two-way ANOVA: $^{**}P < 0.01$ and $^{***}P < 0.001$.

DISCUSSION

In this study, we have identified a pM binding-affinity antibody 4B1 with high specificity for TCR–CD3 complex. Compared to OKT3, this antibody exhibits reduced cytokine release and more potent tumor cell killing ability both *in vitro* and in mouse xenograft models when constructed in the BsAb format. The cryo-EM structure of 4B1 Fab in complex with the intact TCR–CD3 revealed that 4B1 Fab specifically binds to the CD3ε subunit of CD3δ/ε. This is in sharp contrast with OKT3 Fab which interacts with both CD3ε chains of TCR–CD3. Structural comparison indicates that steric-based antibody recognition blocks 4B1 from binding to the CD3ε subunit of CD3γ/ε. Collectively, OKT3 binds to the TCR complex with high avidity, causing more TCR clustering and strong T cell activation with

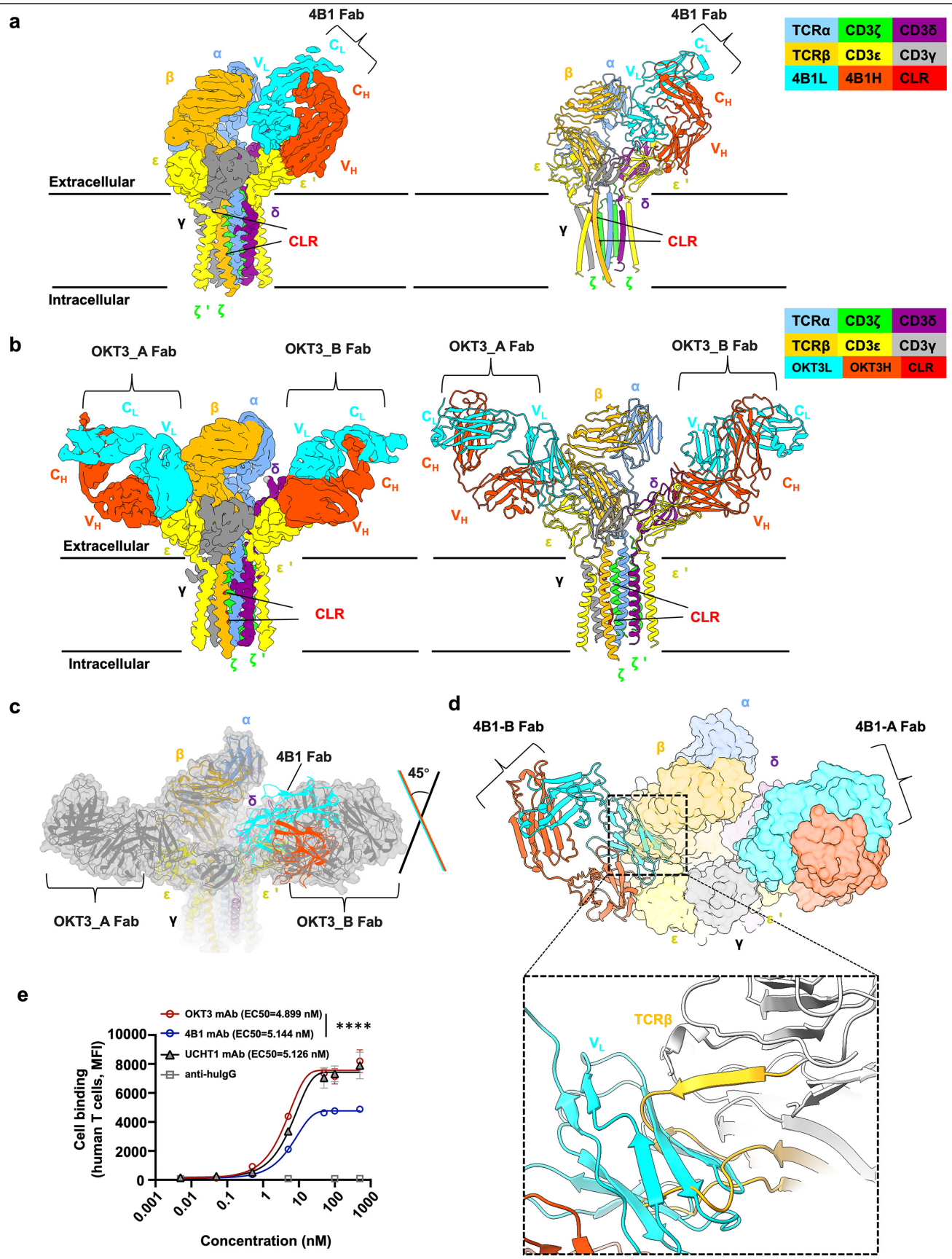

Fig. 4 Structural comparison between 4B1- and OKT3-bound TCR–CD3 complexes. a EM density and cartoon representation of TCR–CD3 in complex with 4B1 Fab. TCRα, TCRβ, CD3ε, CD3γ, CD3δ, CD3ζ, CLR, 4B1L and 4B1H are shown in blue, orange, yellow, gray, purple, green, red, cyan, and orange red, respectively. CLR: cholesterol. **b** EM density and cartoon representation of TCR–CD3 in complex with OKT3 Fab. The TCRα, TCRβ, CD3ε, CD3γ, CD3δ, CD3ζ, CLR, OKT3L and OKT3H are shown in blue, orange, yellow, gray, purple, green, red, cyan, and orange red, respectively. **c** Structural comparison of TCR–CD3–4B1 and TCR–CD3–OKT3. TCR–CD3–4B1 is colored as **a**, and TCR–CD3–OKT3 is colored gray. **d** 4B1 sterically clashes with the TCRβ subunit when interacting with the other site bound by OKT3. The TCR–CD3–4B1 complex is shown as surface and colored as in **a**. **e** 1×10^7/mL purified human $CD3^+$ T cells were incubated for 30 min with increasing doses of OKT3 and 4B1 mAbs, and anti-human IgG as an isotype control. The cells were then labeled with anti-human IgG-FITC secondary antibodies. The MFI of antibody binding to human T cells was detected by flow cytometry dependent on antibody concentrations. Data are presented as mean ± SEM, $n = 3$. Statistical significance was calculated with two-way ANOVA: $^{****}P < 0.0001$.

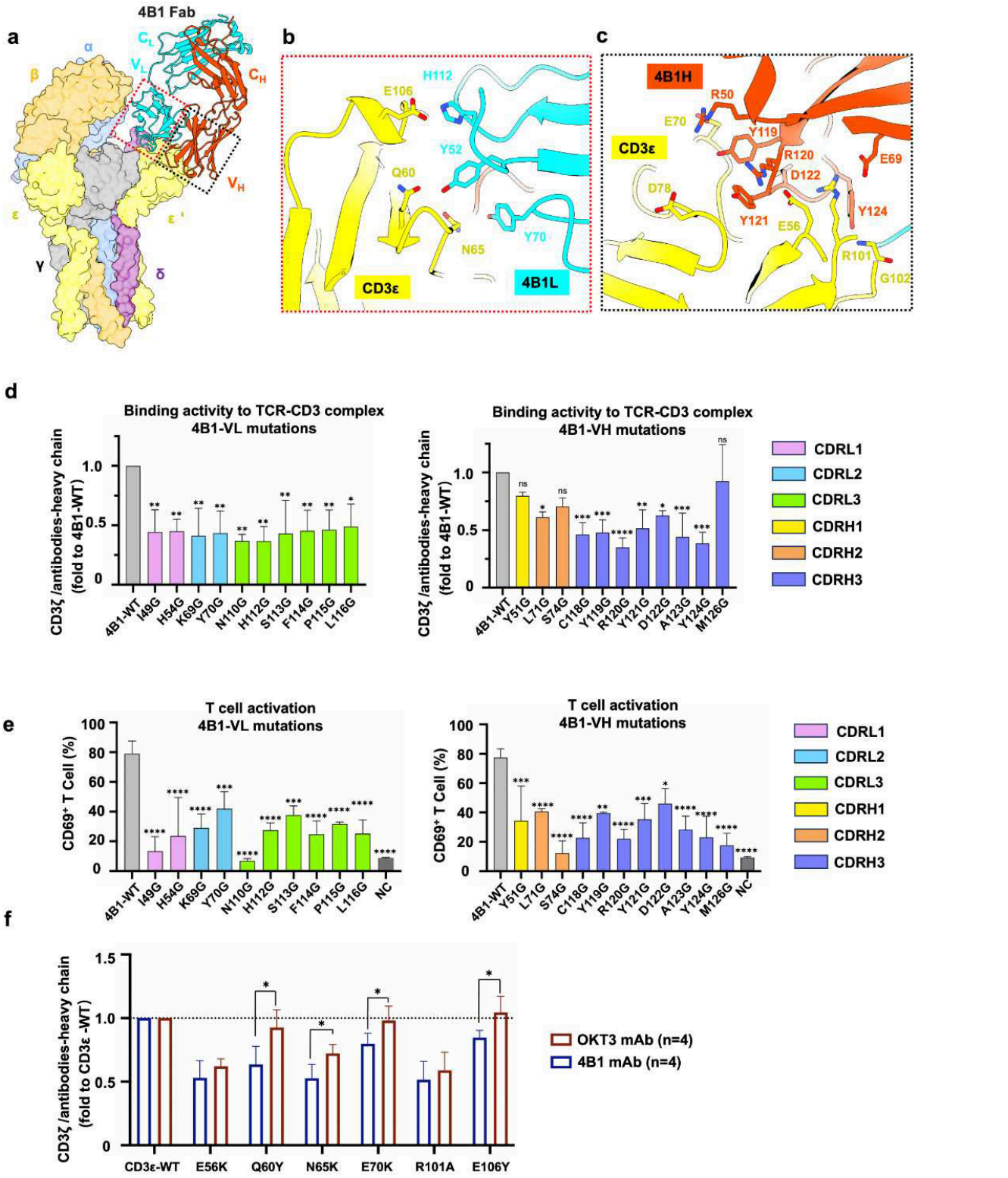

Fig. 5 The interface between 4B1 and TCR–CD3 complexes. a Cartoon representation of the TCR–CD3–4B1 complex. For clarity, the antibody 4B1 is shown in cartoon. The TCR–CD3 is represented by transparent surface. The interfaces involved in the assembly of the TCR–CD3 and 4B1 are highlighted using dotted quadrilateral. **b**, **c** Details of the interfaces between TCR–CD3 and the light chain (**b**), heavy chain (**c**) of antibody 4B1. The residues of 4B1 surrounding TCR–CD3 are labeled and shown in sticks. **d** To quantify the binding activity of 4B1 wild-type (WT) and mutant antibodies to the TCR–CD3 complex, a TCR pull-down assay was performed. The relative binding affinity was determined by measuring the ratio of co-precipitated CD3ζ to the heavy chain of each antibody (4B1-WT or mutant). For each set of mutants (vL, left; vH, right), the binding levels were normalized to that of the 4B1-WT control, which was set to 1. Data are presented as mean ± SEM, $n = 3$. Statistical significance was calculated with one-way ANOVA: $^{*}P < 0.05$, $^{**}P < 0.01$, $^{***}P < 0.001$ and $^{****}P < 0.0001$. ns, not significant. **e** 1×10^6/mL human $CD3^+$ T cells were incubated with 5μg/mL 4B1-mutant mAbs for 24 h (NC: human $CD3^+$ T cells without activation). The percentage of $CD69^+CD3^+$ T cells was measured. The percentage of $CD69^+$ T cells in each 4B1 mutant group was compared with WT 4B1. Data are presented as mean ± SEM, $n = 3$. Statistical significance was calculated with one-way ANOVA, $^{*}P < 0.05$, $^{***}P < 0.001$ and $^{****}P < 0.0001$. **f** The binding activity of 4B1 and OKT3 antibodies for WT and CD3ε mutant TCR–CD3 complexes was evaluated by a TCR pull-down assay. For each antibody, the relative binding level was quantified as the ratio of co-precipitated CD3ζ to its heavy chain and normalized to the value obtained with the WT TCR–CD3 complex (set to 1). Data are presented as mean ± SEM, $n = 4$. Statistical significance was determined by one-way ANOVA test, $^{*}P < 0.05$.

high cytokine release. In contrast, 4B1 binds with low avidity to the TCR–CD3 complex, causing less TCR clustering and delayed, weaker T cell activation, and significantly reduced cytokine release.

The differences in T cell activation phenotypes induced by 4B1 and OKT3 are reminiscent of the activation of cytotoxic T lymphocytes induced by low and high concentrations of pMHC complexes, respectively[55,56]. The activation of cytotoxic T lymphocytes requires the presence of two thresholds: one for polarized granule secretion and the other for cytokine production[56]. Interestingly, the threshold for target cell lysis during activation is over 1,000-fold more sensitive than the threshold for cytokine release. This was shown to arise from the differences in the concentration of pMHC complexes on the target cell surface and the number of pMHC–TCR complexes formed. Similarly, lowering the concentrations of OKT3 greatly reduces production of cytokines. These results appear to suggest that more efficient cytokine release triggered by OKT3 is associated with its lower TCR–CD3 affinity than 4B1. However, the high TCR–CD3 binding affinity antibodies UCHT1 and SP34 also exhibit CRS[35,57,58]. These data suggest that alternative and/or additional mechanisms operate to limit 4B1-triggered cytokine production while maintaining its potent tumor cell killing activity. Our structural data suggest the mechanism by which 4B1 triggers biased activation of T cells. Specific binding of 4B1 to a single CD3ε subunit of CD3δ/ε is likely to be important for the biased activation of the potent tumor cell killing activity of 4B1. It might be that the specific binding with low avidity renders the threshold for cell killing activity much more sensitive than the threshold for 4B1-induced cytokine release. Thus, a larger buffer region exists between the two thresholds to ensure effective activation of tumor cell killing activity while minimizing excessive cytokine secretion. Consistently, our study demonstrated that UCHT1, which exhibits pM binding-affinity for the TCR complex and binds to both CD3ε subunits, is also significantly more potent in inducing cytokine release from T cells. The discovery of high affinity antibody 4B1 challenges the prevailing notion that TCR activation antibodies with higher affinity are correlated with a more cytokine release than lower affinity counterparts. Our findings demonstrate that TCR activation antibodies with higher affinities are not necessarily correlated with a more severe cytokine release when compared with lower affinity counterparts.

In this study, we used systemic cytokine levels as a key indicator of CRS risk in humanized mouse models. This approach is widely adopted in preclinical development of T cell engagers to evaluate inflammatory potential[59-61]. While cytokine elevation remains a central biomarker of CRS, we acknowledge that clinical CRS is a complex syndrome whose severity depends on a constellation of physiological responses, including fever, hypotension, and organ injury[60,62]. Future studies employing more integrated models that monitor physiological parameters in addition to cytokines could further delineate the safety profile of 4B1 *in vivo*.

Treatment with T-BsAb can cause depletion of T cells due to increased expression of immune-checkpoint components[63]. This has been exemplified by the Teplizumab mAb and the Blinatumomab T-BsAb, both of which use the OKT3 scaffold[64,65]. T cell exhaustion signifies a potential immune evasion mechanism[66]. In contrast to the widely used OKT3, both mAb and BsAb forms of 4B1 have demonstrated the ability to expand T cells to a greater extent *in vitro* and in humanized mice. Conventional anti-CD3 antibodies (e.g., OKT3) often cause overactivation, driving T cells toward exhaustion or senescence. Using an anti-CD3 antibody to minimize T cell exhaustion while enhancing expansion capacity could be a promising strategy to address the critical barriers of exhaustion and senescence in CAR-T cell production and therapy. Furthermore, 4B1 induced less T cell exhaustion than OKT3, as evidenced by the reduced expression of exhaustion markers such as PD-1 and Tim-3, This could be partially attributed to its lower level of cytokine release. Indeed, cytokines like IL-10, IL-6, and IL-2 have been implicated in T cell exhaustion[67,68]. It is worth investigating whether the enhanced proliferation of T cells and the reduced level of exhaustion mediated by 4B1 BsAbs are associated with its more potent tumor-killing effect than OKT3 BsAbs.

The IgG-scFv and CrossMab formats of bispecific antibodies engage T cells through fundamentally distinct avidity mechanisms: the IgG-scFv can directly cross-link TCRs via its bivalent anti-CD3 arm, whereas the CrossMab relies on antigen-dependent, multivalent binding to bring TCRs into proximity (Supplementary Fig. S7a, b). Despite these architectural differences, both formats yield a consistent functional outcome: the 4B1 arm, owing to its 1:1 binding stoichiometry, induces markedly lower inflammatory cytokine release than the OKT3 arm, independent of the bispecific architecture. This is because 4B1's constrained binding geometry intrinsically limits TCR-cluster consolidation and signal amplification at the immune synapse relative to OKT3.

In addition, our results suggest that, despite OKT3 having a lower affinity with TCR–CD3 complex, it triggers higher level of T cell exhaustion due to its binding to both CD3ε chains of the TCR, whereas 4B1 binds to only one. In summary, the lower level of exhaustion observed with 4B1 supports the notion that the degree of exhaustion is more dependent on the number of bound antibodies (avidity) rather than their binding affinity. Consistently, a recent study by Singhaviranon *et al*. reported that T cell exhaustion is dependent on TCR avidity rather than TCR affinity[69]. Low-avidity T cells are the sole mediators of cancer control in mice and are exclusively responsive to checkpoint blockade in both mice and humans. In contrast, high-avidity T cells are not only ineffective but also immune-suppressive. The underlying mechanism for these differences is attributed to the higher exhaustion status of high-avidity T cells.

The intracellular mechanisms underlying the distinct T cell activation phenotypes of 4B1 (termed Granzyme/perforin-cytokine decoupled antibody, GCDAb) and OKT3 remain to be determined. OKT3 Fab binds to two epitopes on the TCR–CD3 complex, whereas 4B1 Fab binds to only one epitope. Consequently, a possible mechanistic explanation is that OKT3 is more likely to cause TCR–CD3 complex clustering or form larger clusters. When the extent of clustering exceeds a threshold, it generates stronger transmembrane activation signals, thereby initiating the transcription and secretion of more inflammatory cytokines. In contrast, a small amount of TCR–CD3 complex clustering may mainly activate effector functions, such as the release of Granzyme and perforin. Thus, CRS may be dependent on the amount of TCR clustering. 4B1, by binding to a single TCR–CD3 epitope, may trigger finely tuned intracellular signaling cascades compared to OKT3. This mechanism ensures that T cells can mount a moderate response when encountering low levels of antigen,

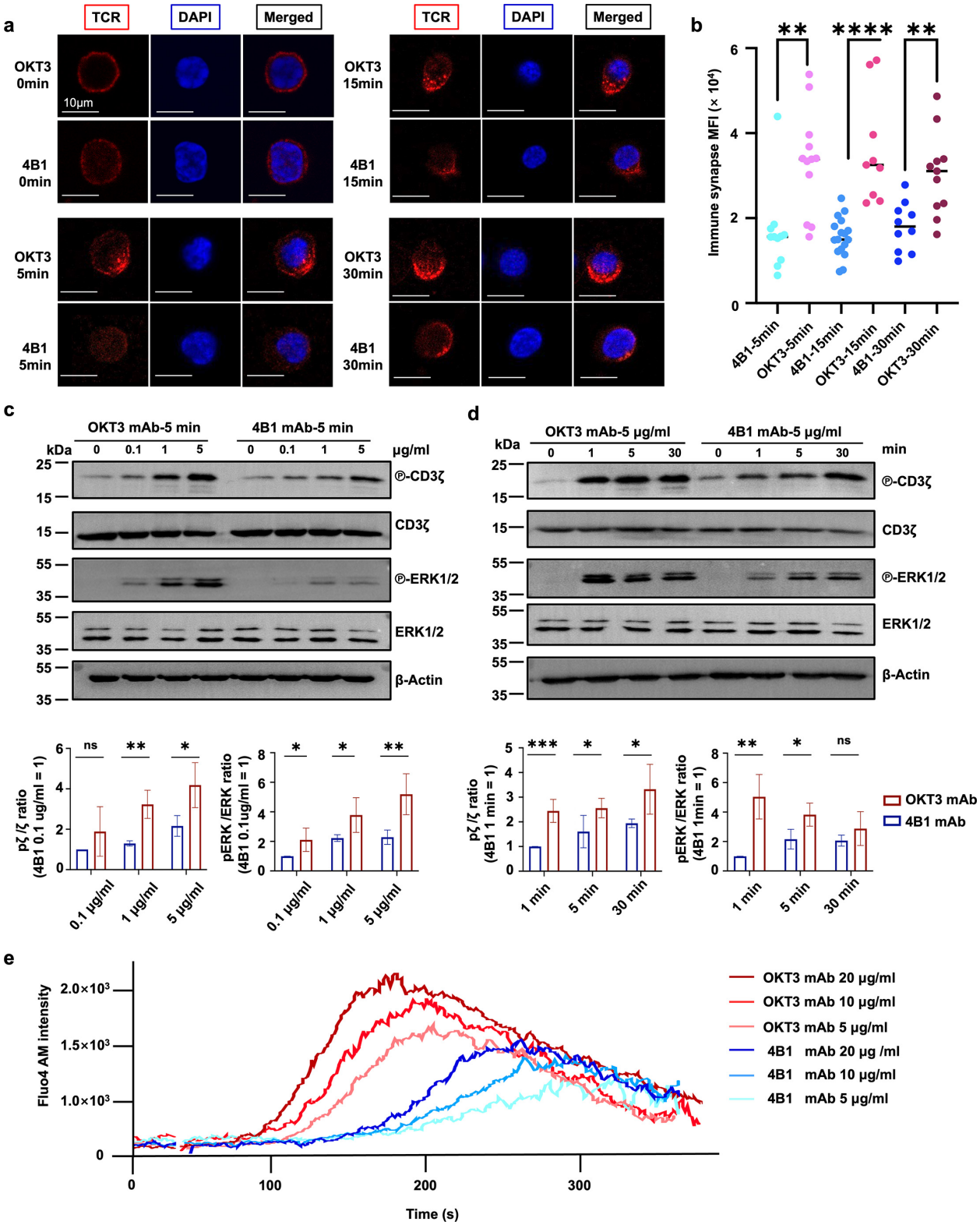

Fig. 6 TCR clustering mediated by OKT3 or 4B1 antibodies triggers differential downstream signaling. a Representative confocal image of human CD3$^+$ T cells stimulated with OKT3 or 4B1 mAb at the indicated incubation time points, showing TCR (red), DAPI (blue), and merged images. Scale bar = 10 μm. **b** Quantification of the antibody's median fluorescence intensity of antibody-to-antibody area. Data are presented as mean ± SEM, *n* = 9–17. Statistical significance was calculated using multiple unpaired *t*-test: ** $P < 0.01$, **** $P < 0.0001$. **c**, **d** Immunoblot analysis of phosphorylated CD3ζ (pY142) and Erk (pT202Y204/pT185Y187) in human T cells. **c** Cells were stimulated with indicated concentrations of OKT3 or 4B1 for 5 min (top panel); the corresponding ratios of pCD3ζ/CD3ζ and pERK/ERK are shown in the bottom panel. **d** Cells were stimulated with 5 μg/mL OKT3 or 4B1 for the indicated time points (top panel); the corresponding ratios are shown in the bottom panel. Band intensities were quantified and normalized, with 4B1-0.1 μg/mL set as 1 (**c**) and 4B1-1 min set as 1 (**d**). Data are presented as mean ± SEM, *n* = 3–4. Statistical significance was calculated with multiple unpaired *t*-test: * $P < 0.05$, ** $P < 0.01$ and *** $P < 0.001$. ns, not significant. **e** Analysis of intracellular calcium signals in CD3$^+$ T cells stimulated with the indicated concentrations of OKT3 and 4B1.

where low level of TCR activation may preferentially trigger cytotoxicity (direct killing), avoiding excessive inflammation[70]. In the presence of high levels of antigen, T cells can mount a strong response to eliminate infection. It is also an interesting question to consider whether the differential activation of T cells is regulated by components within the T cell itself.

In conclusion, we have identified a highly specific TCR–CD3 antibody 4B1 and characterized it using structural, biochemical, and functional analyses. The *in vitro* and *in vivo* data from these assays have revealed the molecular mechanisms underlying biased activation of T cells in terms of cytolytic activity and T cell expansion. These discoveries offer valuable insights for developing next-generation mAbs and T-BsAbs targeting the TCR–CD3 complex, enabling either high-efficiency T cell expansion or potent cytolytic activity while minimizing CRS effects for clinical use.

MATERIALS AND METHODS

Cell lines

Four human tumor cell lines were used. Human gastric carcinoma cell line MKN45 (National Infrastructure of Cell Line Resource), human colon adenocarcinoma cancer cell line LOVO (Nanjing SenBeiJia Biological Technology Co., Ltd.), human ovarian cancer cell line HELA (National Infrastructure of Cell Line Resource) and human Burkitt's lymphoma stable-express luciferase cancer cell line Raji-Luc (Shanghai Fu Heng Biotechnology Company) were cultured in 1640 (Gibco) supplemented with 1% L-glutamine, 50 U/mL penicillin / streptomycin (Gibco) and 10% fetal bovine serum (FBS, Gibco) at 37 ℃ with 5% CO_2. HEK-293F cell line (Invitrogen) was cultured in SMM 293-TII serum-free medium (Sino Biological, CHINA) at 37 ℃ with 5% CO_2.

Mouse immunization

To generate monoclonal antibodies against the TCR–CD3 complex, BALB/c mice (purchased from ChangSheng Company, Liaoning, China) were immunized intraperitoneally with 50 μg of full-length TCR–CD3 protein. The immunization schedule consisted of four injections: the primary immunization used antigen emulsified in incomplete Freund's adjuvant, followed by three booster immunizations at 7-day intervals. The procedure was completed on day 28, and final serum samples were collected.

Serum titer determination by enzyme-linked immunosorbent assay (ELISA)

Antibody titers in mouse serum were assessed by ELISA. Briefly, 96-well plates were coated with 0.2 μg of full-length TCR–CD3 protein and incubated overnight at 4 ℃. Plates were then blocked for 2 h at room temperature with blocking buffer (5% skim milk in 1× PBS buffer). Serial dilutions of serum (1:500 to 1:32 × 10^4) prepared in blocking buffer were added to the antigen-coated wells. After incubation, plates were probed with horseradish peroxidase-conjugated secondary antibody, developed with a chemiluminescent substrate, and luminescence was quantified using a plate reader. Sera that produced a detectable signal at a dilution of 1:32 × 10^4 were considered positive.

Antigen-specific B-cell sorting by flow cytometry

Lymphocytes were isolated from spleens of immunized mice. For staining, cells were first incubated with anti-mouse CD16/CD32 antibody (2.5 μg/mL) for 15 min at 4 ℃ to block Fc receptors. Cells were then stained in buffer with anti-mouse CD19 antibody (1 μg/mL), biotinylated antigen (2 μg/mL) for 30 min at 4℃. After two washes with PBS containing 2% FBS and 2 mM EDTA, cells were stained with streptavidin-PE and streptavidin-APC for 15 min, washed again, and resuspended in PBS (2% FBS, 2 mM EDTA). Antigen-binding (PE^+/APC^+) $CD19^+$ single B cells were sorted into 96-well plates using a flow cytometer.

Variable region amplification, sequencing, and recombinant expression

Variable regions of heavy-chain (vH) and light-chain (vL) genes from single sorted B cells were amplified by 5′-RACE PCR. The vH and vL fragments were separately cloned into a mammalian expression vector, pcDNA3.4, containing a human leader sequence and the constant region of human IgG1 Fc. Full-length antibody constructs were transiently transfected into HEK293F cells, and antibodies were purified by Protein A affinity chromatography. Purified antibodies were tested for binding to TCR–CD3 complex using the ELISA procedure described above. Clones showing positive ELISA signals were subjected to next-generation sequencing to confirm their variable region sequences.

Generation of monoclonal antibodies and bispecific antibodies

The variable domains of anti-CEA, anti-CD19, and anti-CD3 antibodies were from T84.66[71], B43[72], and OKT3[73], respectively. 4B1 antibody was obtained by screening in our laboratory.

IgG-based proteins have a human IgG1 framework that contained both L234A L235A and P329G mutations to silence Fc receptor and complement binding activities.

By cloning the antibody sequence into the mammalian expression vector pcDNA3.4, the UCHT1 IgG1 mAb[41], OKT3 IgG1 mAb and 4B1 IgG1 mAb were obtained. All three are chimeric antibodies comprising murine variable regions and human IgG1 constant regions (CL and CH1-CH3 domains). The constant regions contain Fc-silencing mutations to eliminate Fc receptor binding.

The heavy and light chains of BsAbs were constructed in two vectors, respectively. For the OKT3/anti-TAA or 4B1/anti-TAA IgG-scFv constructs, the scFv fragment of the TAA-specific antibody was fused to the C-terminus of the OKT3 or 4B1 heavy chain using a short "G_4S_1" linker. The vH and vL domains within the anti-TAA scFv were joined by a flexible $(G_4S_1)_4$ linker to ensure proper folding and domain pairing. For OKT3×anti-TAA, 4B1×anti-TAA BsAb: OKT3-IgG1, 4B1-IgG1 and TAA-IgG1 form clones were constructed respectively. The CH3 part of OKT3-IgG1 and 4B1-IgG1 heavy chain adopted hole mutation, and the CH3 part of TAA-IgG1 heavy chain adopted knob mutation. Both parts were expressed together to form a heterodimeric "knob-hole".

Protein expression and purification

- ***Monoclonal and bispecific antibody purification***

Monoclonal and bispecific antibodies were expressed in HEK-293F cells. Briefly, for OKT3/anti-TAA, 4B1/anti-TAA form BsAbs, heavy and light chain plasmids were co-transfected in a 1:1 ratio in 1 μg DNA/mL medium. For OKT3×anti-TAA, 4B1×anti-TAA form BsAb, the transfected HEK-293F cells were co-transfected with OKT3 or 4B1 heavy chain plasmid and TAA heavy chain plasmid and light chain plasmid in 1 μg DNA/mL medium at a ratio of 1:1:1. The transfected HEK-293F cells were cultured in a 5% carbon dioxide (CO_2) incubator at 37 ℃ for 3 days with vibration. The supernatant was centrifuged at 10,000 rpm for 5 min and filtered through a 2 μm filter. The antibody proteins were purified from the supernatant binding protein A beads. Subsequent superdex 200 increase GL

column evaluation revealed high purity and lack of aggregated (< 1%) antibody proteins.

• ***TCR–CD3 complex purification***

Plasmids encoding the WT or mutant TCR–CD3 complex were transfected into HEK-293F cells in 1 μg DNA/mL medium. The culture was diluted to 1.2 × 10^6 cells/mL, and at 24 h post-transfection, valproic acid was added to a final concentration of 11 mM. Cells were harvested after 60 h of total expression. Cell pellets from two liters of culture were resuspended in a low-salt HEPES buffer (25 mM, pH 7.5) supplemented with 1 mM PMSF and subjected to repeated Dounce homogenization. The membrane fraction was subsequently washed with a high-salt HEPES buffer (25 mM, pH 7.5, 1 M NaCl) and then solubilized for 2 h at 4 °C in buffer A (25 mM HEPES, pH 7.5, 150 mM NaCl, 1% DDM, 1 mM PMSF). After clearing the lysate by centrifugation (40,000× *g*, 30 min), the supernatant was incubated with streptactin resin for 2 h at 4 °C.

The resin was washed with buffer B (25 mM HEPES, 300 mM NaCl, 0.025% digitonin), and the protein was eluted with buffer C (25 mM HEPES, 150 mM NaCl, 0.06% Glyco-digitonin, 4 mM desthiobiotin). The eluate was concentrated and subjected to size-exclusion chromatography (Superose 6 Increase) in buffer D (25 mM HEPES, 150 mM NaCl, 0.025% Glyco-digitonin). Protein purity was assessed throughout the purification by SDS-PAGE and Coomassie blue staining.

Bio-layer interferometry assay

The bio-layer interferometry assay was performed at 30 °C on the Octet RED96 System (ForteBio) with 25 mM HEPES (pH 7.5), 150 mM NaCl and 0.02% GDN as the running buffer. The purified TCR–CD3 protein was biotinylated using NHS-LC-LC-Biotin (Thermo Fisher Scientific) and then loaded onto streptavidin biosensors (ForteBio) that had been equilibrated in the running buffer for 10 min. Subsequently, the biosensors were equilibrated in the binding buffer (1640 medium) for 120 s, followed by incubation with serial dilutions of antibodies (UCHT1, OKT3, 4B1) ranging from 8 to 64 nM, with the binding time set to allow saturation at 64 nM, and then a 300-second dissociation step. The data were analyzed using the global fitting algorithm included in the Octet Data Analysis Software v.9.0 (ForteBio).

T-cell activation assay

Human PBMCs were isolated from leukopacks by ficoll separation (TBD). All experiments involving human PBMC were in accordance with ethics in medicine guidelines for the Harbin Institute of Technology (No: HIT-2023066). Naïve human T cells were purified using human T cell isolation kit (Stem cell). To quantify T cell activation, we stimulated the purified naïve human T cells for 24 h using different antibodies with the indicated stimulation doses. After 24 h, cell pellets were surface stained with an CD69-APC antibody (Biolegend) and analyzed with a BD LSR Fortessa and analyzed in FlowJo software.

Flow cytometric analysis and intracellular cytokine staining

Cell surface staining: $CD3^+$ T cells were washed with 1× PBS and stained for cell surface APC-CD69 (Biolegend) on ice for 20 min in 1× PBS containing 2% FBS. After washing in 1× PBS samples, data were acquired on a BD LSR Fortessa cytometer and analyzed by FlowJo software.

Intracellular cytokine staining: $CD3^+$ T cells were incubated with an increasing dose of mAbs before addition of 10 μg/mL brefeldin A to the culture medium for a further 6 h. To stain surface markers, cells were washed and labelled with antibodies targeting CD3 in 1× PBS for 15 min in the dark at 4 °C, washed and then fixed and permeabilized with BD Cytofix/Cytoperm reagent (BD Biosciences) for 20 min at 4 °C. Cells were stained with anti-GZMB (Biolegend) and anti-perforin in permeabilization solution (BD Biosciences) for 25 min and washed before flow cytometry analysis. Data were acquired on a BD LSR Fortessa cytometer and analyzed by FlowJo software.

***In vitro* cytotoxicity**

3 × 10^4 tumor cells expressing specific TAA were seeded in each well of 96-well plate. 3 × 10^5 isolated human $CD3^+$ T cells or PBMCs were added to each well with tumor cells, treated with a series of dilution of OKT3 BsAb, 4B1 BsAb or control BsAb that cannot bind to specific tumor cell lines. After incubation at 37 °C for 24 h, the cytotoxicity was measured by the lactate dehydrogenase (LDH) release assay using LDH Cytotoxicity Assay Kit (Beyotime).

Measurement of cytokines

3 × 10^5 isolated human T cells were pre-incubated with OKT3-BsAbs or 4B1-BsAbs for 25 min and then washed twice with 1× PBS. Pre-incubated T cells and 3 × 10^4 tumor cells (E: T=10:1) were plated in 96-well plates for 24–48 h. Then supernatant was collected to measure T cell-released cytokines. Serum samples from the animal experiment (2, 6 and 24 h after the first BsAb dose) were used to measure *in vivo* cytokine production. Human T cell-released cytokines including IL-2, IL-6, IL-10, IFN-γ, and TNF-α were measured using LEGENDplex™ Human Th1 Panel (BioLegend) *in vitro* and *in vivo* and analyzed by flow cytometry. Briefly, supernatants were diluted 10-fold and serum samples were diluted 2-fold, and then mixed with appropriate amounts of sample buffer and prelabeled cytokine beads. After 2 h of shaking and incubation at room temperature, samples were washed and the biotinylated secondary antibodies were added. Following a 1 h incubation, PE-labeled streptavidin was added directly. After 30 min, samples were washed, acquired using a BD LSR Fortessa flow cytometer and analyzed using FlowJo software.

Mice

NKG female mice (NOD-*Prkdc*^{scid}*IL-2rg*$^{em1/Cyagen}$, purchased from Cyagen), aging 6 to 8 weeks at the start of the experiment, were maintained under specific pathogen-free conditions with daily cycles of 12 h light/12 h darkness according to the committed guidelines. After arrival, animals were maintained for 1 week for observation and for adaptation to the new environment. All animal experiments were in accordance with Institutional Animal Care and Use Committee (IACUC) guidelines for the University of Harbin Institute of Technology (No: IACUC-2023097).

Xenogenic tumor model

For Raji-Luc tumor xenogenic model,6–8-week-old NKG mice were engrafted with 5 × 10^5 human Raji-Luc cell by intravenous injection (day 0), and after 7 days, 1.5 × 10^7 PBMCs (pre-incubated) were administered by tail intravenous injection (day 7). Mice were treated with 10 μg of OKT3×anti-CD19 or 4B1×anti-CD19 BsAbs, or with 10 μg of OKT3 or 4B1 mAb alone, each in 200 μL of 1× PBS per mouse, as indicated, by

intravenous injection on days 10, 14, 18 and 22 after tumor implant.

To measure Raji-Luc tumor burden, NKG mice were injected intraperitoneally with 150 mg/kg of the luciferase substrate D-luciferin (APE×BIO), suspended in 1× PBS. Ten minutes later, Bioluminescence Imaging (BLI) of the mice was performed under isoflurane anesthesia using the Xenogen IVIS system (PerkinElmer). Image acquisition was carried out with the field of view set to a subject height of 1.5 cm, medium binning level, and a fixed exposure time. BLI signals were extracted using the Living Image Software (Xenogen). Regions of interest were drawn around each tumor mass, and photon intensities were recorded as p/s/cm^2/sr. These mice were imaged on each time point as indicated.

Grid preparation and cryo-EM data collection

All samples were applied to glow-discharged holey Au 300 grids (Quantifoil R1.2/1.3). The grids were vitrified in liquid ethane using a FEI Vitrobot Mark IV. The Vitrobot was operated at 4 °C, with a blot force of "0–5", and a blotting time of 1–6 s, and 100% humidity. Cryo-grids were first screened on a FEI 200 kV transmission electron microscope (Talos Arctica equipped with a FEI Falcon 3 camera). Data collection of TCR–CD3–4B1 complex was taken by a Falcon 3 detector operated at 300 kV (FEI Titan Krios) using the Thermo Fisher Scientific EPU software. The nominal magnification of 96,000× and the defocus range between −1.5 and −2.5 µm were used for data collection. For each image stack (32 frames), a total dose is about 40.0 electrons/Å^2 at a calibrated pixel size 0.86 Å. The datasets of TCR–CD3–OKT3 complex were collected by a Gatan K2 detector operated at 300 kV. The energy filter slit was set to 20 eV. The nominal magnification of 215,000× and the defocus range between −1.5 and −2.5 µm were used for data collection. For each image stack (40 frames), a total dose is about 60.0 electrons/Å^2 at a calibrated pixel size 0.335 Å.

Cryo-EM data processing

For the dataset of TCR–CD3–4B1, a total of 6,336 micrographs were obtained for data processing (Supplementary Fig. S3). Movie stacks were drift-corrected, electron-dose weighted, and two-fold binned using MotionCor2[74]. The contrast transfer function (CTF) parameters of drift-corrected micrographs were estimated by the program CTFFIND4[75]. A total of 2,921,005 particles were automatically picked in Relion[76]. Then, the particles were extracted with 4× binning (3.44 Å per pixel) and subjected to three rounds of 2D classifications and one round of 3D classification, yielding a total of 439,348 particles for the final reconstruction. After the CTF refinement and Bayesian polishing, the final density map was reconstructed at a resolution of 3.14 Å. The resolution was evaluated based on the gold standard Fourier shell correlation (threshold = 0.143), and the local resolution map was estimated by cryoSPARC.

For the dataset of TCR–CD3–OKT3, a total of 18,738 micrographs were obtained for data processing (Supplementary Fig. S4). Movie stacks were drift-corrected, electron-dose weighted, and two-fold binned using MotionCor2. Then, the drift-corrected micrographs were imported into cryoSPARC for CTF estimation. A total of 5,496,886 particles were automatically selected using Blob picker in cryoSPARC. Then, the particles were extracted with 2× binning (1.34 Å per pixel) and subjected to two rounds of 2D classifications to remove junk particles. About 100,000 particles were selected for ab initio reconstruction to generate initial model. All resulting 1,309,456 particles were then used for two rounds of heterogeneous refinement with seven classes. A total of 502,960 particles from the best class were subjected into non-uniform refinement and yielded a reconstruction at 3.18 Å overall resolution. The resolution was evaluated based on the gold standard Fourier shell correlation (threshold = 0.143), and the local resolution map was estimated by cryoSPARC.

Model building and structure refinement

For the structures of TCR–CD3–4B1 and TCR–CD3–OKT3 complexes, model building was carried out based on the 3.14 Å and 3.18 Å reconstruction maps, respectively (Supplementary Figs. S3, S4). The models of TCR–CD3 (PDB 6JXR), and OKT3 Fab (PDB 1SY6) were manually fitted into the density maps by CHIMERA[77], followed by manual adjustment using COOT[78]. The model of 4B1 Fab was built *de novo* and refined using phenix. real_space_refine[79] with secondary structure and geometry restraints. The final models were evaluated by MolProbity[80] and Ramachandran plot[81]. Statistics of the map reconstruction and model refinement are presented in Supplementary Table S2. Structural figures were prepared with ChimeraX.

Cell binding dose curves

Human T cells were harvested, washed, and resuspended in 50 µL 1× PBS buffer containing 2% FBS. 5 × 10^5 cells were incubated for 30 min at 4 °C with increasing doses of antibodies, anti-human-IgG was used as isotype control. After the incubation, cells was washed and incubated with FITC anti-human IgG Fc antibody (Biolegend) for 30 min at 4 °C and subsequently washed again. The fluorescence associated with cells was acquired on a BD LSR Fortessa cytometer and analyzed by FlowJo software.

Preparation of iFluor-555-conjugated antibodies

The conjugation of iFluor-555 (AAT Bioquest) to antibodies was performed according to the manufacturer's instructions. Briefly, 293F cells expressing OKT3 or 4B1 mAb were mixed at a 1:10 molar ratio with 2 mM iFluor-555 and incubated for 1 h with slight rotation at room temperature. Excess iFluor-555 was removed using a Zeba Spin Desalting column (Thermo Fisher Scientific) and the conjugated antibody was eluted in 1× PBS.

Microscopy imaging and analysis

To image TCR clustering, 3 × 10^5 human T cells were harvested from culture and resuspended in 30 µL 1× PBS (supplemented with 5 µg/mL iFlour-555 conjugated OKT3 or 4B 1 mAb). After incubation for 5–30 min, the cells were washed with 1× PBS, resuspended in 200 µL 1× PBS and transferred into 20-mm-diameter imaging dishes (NEST). Then T cells were fixed with 1% paraformaldehyde for 30 min at room temperature. After washing with 1× PBS, T cells were permeabilized with 0.1% Triton X-100 for 15 min and then blocked with 1% (w/v) bovine serum albumin for 1 h at room temperature. Dishes were washed and mounted with Antifade Mounting Medium with DAPI (Beyotime).

Imaging was performed using a ZEISS LSM880 confocal laser scanning microscope. Images were captured using a 100× objective. All images were analyzed and processed consistently using ImageJ software. The degree of TCR clustering was quantified based on the intensity of fluorescently labeled

proteins in the plasma membrane. The immune synapse was selected by manually drawing a region and the average fluorescence intensity of the immune synapse was divided by the area of immune synapse to calculate the degree of TCR clustering.

TCR pull-down assay

To assess binding activity, purified WT or mutant antibodies (7 μg of 4B1 or OKT3) bound to proteinA-Sepharose beads were incubated with a 15 μg WT or mutant TCR–CD3 complexes at 4 °C for 30 min. The beads were subsequently washed three times with a wash buffer (25 mM HEPES, 150 mM NaCl, 0.025% Glyco-digitonin, pH 7.5). The co-precipitated proteins were then analyzed by SDS-PAGE and Coomassie blue staining, and band intensities were quantified using ImageJ software.

Quantification and statistical analysis

Data between two groups were compared using a two-tailed unpaired or paired Student's *t*-test, as appropriate based on data distribution. For dose-response curve comparisons, two-way ANOVA test was performed to compare the two curves. For comparisons involving more than two groups, one-way ANOVA test was used. Survival curves were compared using the log-rank test. All results are presented as mean ± SEM unless otherwise stated. All statistical analyses were performed using GraphPad Prism (GraphPad Software Inc.). Differences were considered statisticallysignificant at $P < 0.05$. Significance levels are indicated as $^{*}P < 0.05$, $^{**}P < 0.01$, $^{***}P < 0.001$, and $^{****}P < 0.0001$.

DATA AND MATERIALS AVAILABILITY

The atomic coordinates for 4B1–TCR–CD3 complex have been deposited in the Worldwide Protein Data Bank (PDB) with the accession code 91RU. The corresponding cryo-EM maps has been deposited in the Electron Microscopy Data Bank (EMDB) with the accession code EMD-60821. The atomic coordinates for OKT3–TCR–CD3 complex have been deposited in the Worldwide Protein Data Bank (PDB) with the accession code 91RS. The corresponding cryo-EM maps has been deposited in the Electron Microscopy Data Bank (EMDB) with the accession code EMD-60818. All data described in this paper are present either in the main text or in the supplementary information. Any additional information required to reanalyze the data reported in this paper is available from the lead contact upon request.

ACKNOWLEDGMENTS

We thank the EM platform at School of Life Science and Technology of Harbin Institute of Technology and the cryo-EM facility, the high-performance computing center core facility of Westlake University for providing the supports. This work was supported by the Heilongjiang Provincial Key R&D Program (2025ZX04C01) and the New Cornerstone Investigator Program (NCI202237) to Z.H.

AUTHOR CONTRIBUTIONS

Z.H. conceived, conceptualized and designed the study. Y.C., W.G., A.Z. and C.G. prepared the protein samples for cryo-EM and collected the cryo-EM data. X.L., B.H., E.S. and D.Y. did functional experiments. F.L. performed the PBMC isolation experiments, Y.Z. and Z.L. performed cryo-EM data processing and model building. Z.H. interpreted the data and supervised the study. Z.H., X.L. and Y.Z. wrote the paper with inputs from all authors.

COMPETING INTERESTS

X.L., D.Y., E.S. and Z.H. are named inventors on a related patent application.

REFERENCES

1. Dong, D. et al. Structural basis of assembly of the human T cell receptor-CD3 complex. *Nature* **573**, 546–552 (2019).
2. Wang, J.H. & Reinherz, E.L. The structural basis of αβ T-lineage immune recognition: TCR docking topologies, mechanotransduction, and co-receptor function. *Immunol. Rev.* **250**, 102–119 (2012).
3. Call, M.E., Pyrdol, J. & Wucherpfennig, K.W. Stoichiometry of the T-cell receptor-CD3 complex and key intermediates assembled in the endoplasmic reticulum. *EMBO J.* **23**, 2348–2357 (2004).
4. Dave, V.P. Role of CD3ε-mediated signaling in T-cell development and function. *Crit. Rev. Immunol.* **31**, 73–84 (2011).
5. Wu, W. et al. Multiple signaling roles of CD3ε and its application in CAR-T cell therapy. *Cell* **182**, 855–871.e23 (2020).
6. Rossjohn, J. et al. T cell antigen receptor recognition of antigen-presenting molecules. *Annu. Rev. Immunol.* **33**, 169–200 (2015).
7. Chen, Y. et al. Cholesterol inhibits TCR signaling by directly restricting TCR-CD3 core tunnel motility. *Mol. Cell* **82**, 1278–1287.e5 (2022).
8. Gaud, G., Lesourne, R. & Love, P.E. Regulatory mechanisms in T cell receptor signalling. *Nat. Rev. Immunol.* **18**, 485–497 (2018).
9. Kane, L.P., Lin, J. & Weiss, A. Signal transduction by the TCR for antigen. *Curr. Opin. Immunol.* **12**, 242–249 (2000).
10. Voskoboinik, I., Whisstock, J.C. & Trapani, J.A. Perforin and granzymes: function, dysfunction and human pathology. *Nat. Rev. Immunol.* **15**, 388–400 (2015).
11. Trapani, J.A. & Smyth, M.J. Functional significance of the perforin/granzyme cell death pathway. *Nat. Rev. Immunol.* **2**, 735–747 (2002).
12. Raphael, I., Nalawade, S., Eagar, T.N. & Forsthuber, T.G. T cell subsets and their signature cytokines in autoimmune and inflammatory diseases. *Cytokine* **74**, 5–17 (2015).
13. Ellenhorn, J.D.I., Hirsch, R., Schreiber, H. & Bluestone, J.A. In vivo administration of anti-CD3 prevents malignant progressor tumor growth. *Science* **242**, 569–571 (1988).
14. Chen, H. et al. Self-programmed dynamics of T cell receptor condensation. *Proc. Natl. Acad. Sci. USA* **120**, e2217301120 (2023).
15. Ting, A.Y. & Endy, D. Decoding NF-κB signaling. *Science* **298**, 1189–1190 (2002).
16. Crabtree, G.R. Generic signals and specific outcomes: signaling through Ca^{2+}, calcineurin, and NF-AT. *Cell* **96**, 611–614 (1999).
17. Kuhn, C. & Weiner, H.L. Therapeutic anti-CD3 monoclonal antibodies: from bench to bedside. *Immunotherapy* **8**, 889–906 (2016).
18. Smith, S.L. Ten years of Orthoclone OKT3 (muromonab-CD3): a review. *J. Transpl. Coord.* **6**, 109–121 (1996).
19. Cosimi, A.B. et al. Use of monoclonal antibodies to T-cell subsets for immunologic monitoring and treatment in recipients of renal allografts. *N. Engl. J. Med.* **305**, 308–314 (1981).
20. Ortho Multicenter Transplant Study Group. A randomized clinical trial of OKT3 monoclonal antibody for acute rejection of cadaveric renal transplants. *N. Engl. J. Med.* **313**, 337–342 (1985).
21. Waldron-Lynch, F. et al. Teplizumab induces human gut-tropic regulatory cells in humanized mice and patients. *Sci. Transl. Med.* **4**, 118ra12 (2012).
22. Chatenoud, L. OKT3-induced cytokine-release syndrome: prevention effect of anti-tumor necrosis factor monoclonal antibody. *Transplant. Proc.* **25**, 47–51 (1993).
23. Radhakrishnan, J. & Cohen, D.J. Cytokine-release syndrome: general risk-factor modification-preparation of high-risk patients for use of OKT3. *Trans-*

plant. Proc. **25**, 60–62 (1993).
24. Gaston, R.S. et al. OKT3 first-dose reaction: association with T cell subsets and cytokine release. *Kidney Int.* **39**, 141–148 (1991).
25. Ramos, E.L. et al. Teplizumab and β-cell function in newly diagnosed type 1 diabetes. *N. Engl. J. Med.* **389**, 2151–2161 (2023).
26. Goldman, J.D. & Choi, H. Teplizumab: the first treatment to delay the progression of type 1 diabetes. *Clin. Diabetes* **41**, 474–476 (2023).
27. van de Donk, N.W.C.J. & Zweegman, S. T-cell-engaging bispecific antibodies in cancer. *Lancet* **402**, 142–158 (2023).
28. Bargou, R. et al. Tumor regression in cancer patients by very low doses of a T cell-engaging antibody. *Science* **321**, 974–977 (2008).
29. Goebeler, M.E. & Bargou, R.C. T cell-engaging therapies - BiTEs and beyond. *Nat. Rev. Clin. Oncol.* **17**, 418–434 (2020).
30. Locatelli, F. et al. Effect of Blinatumomab vs chemotherapy on event-free survival among children with high-risk first-relapse B-Cell acute lymphoblastic leukemia: a randomized clinical trial. *JAMA* **325**, 843–854 (2021).
31. Gökbuget, N. et al. Blinatumomab for minimal residual disease in adults with B-cell precursor acute lymphoblastic leukemia. *Blood* **131**, 1522–1531 (2018).
32. Teachey, D.T. et al. Cytokine release syndrome after blinatumomab treatment related to abnormal macrophage activation and ameliorated with cytokine-directed therapy. *Blood* **121**, 5154–5157 (2013).
33. Suntharalingam, G. et al. Cytokine storm in a phase 1 trial of the anti-CD28 monoclonal antibody TGN1412. *N. Engl. J. Med.* **355**, 1018–1028 (2006).
34. Zahid, A., Siegler, E.L. & Kenderian, S.S. CART cell toxicities: new insight into mechanisms and management. *Clin. Hematol. Int.* **2**, 149–155 (2020).
35. Staflin, K. et al. Target arm affinities determine preclinical efficacy and safety of anti-HER2/CD3 bispecific antibody. *JCI Insight* **5**, e133757 (2020).
36. Mandikian, D. et al. Relative target affinities of T-cell-dependent bispecific antibodies determine biodistribution in a solid tumor mouse model. *Mol. Cancer Ther.* **17**, 776–785 (2018).
37. Cuesta, Á.M., Sainz-Pastor, N., Bonet, J., Oliva, B. & Álvarez-Vallina, L. Multivalent antibodies: when design surpasses evolution. *Trends Biotechnol.* **28**, 355–362 (2010).
38. Zuch de Zafra, C.L. et al. Targeting multiple myeloma with AMG 424, a novel anti-CD38/CD3 bispecific T-cell-recruiting antibody optimized for cytotoxicity and cytokine release. *Clin. Cancer Res.* **25**, 3921–3933 (2019).
39. Dang, K. et al. Attenuating CD3 affinity in a PSMAxCD3 bispecific antibody enables killing of prostate tumor cells with reduced cytokine release. *J. Immunother. Cancer* **9**, e002488 (2021).
40. Trinklein, N.D. et al. Efficient tumor killing and minimal cytokine release with novel T-cell agonist bispecific antibodies. *mAbs* **11**, 639–652 (2019).
41. Arnett, K.L., Harrison, S.C. & Wiley, D.C. Crystal structure of a human CD3-ε/δ dimer in complex with a UCHT1 single-chain antibody fragment. *Proc. Natl. Acad. Sci. USA.* **101**, 16268–16273 (2004).
42. Gökbuget, N. et al. Curative outcomes following blinatumomab in adults with minimal residual disease B-cell precursor acute lymphoblastic leukemia. *Leuk. Lymphoma* **61**, 2665–2673 (2020).
43. Verwilghen, J., Baroja, M.L., Van Vaeck, F., Van Damme, J. & Ceuppens, J.L. Differences in the stimulating capacity of immobilized anti-CD3 monoclonal antibodies: variable dependence on interleukin-1 as a helper signal for T-cell activation. *Immunology* **72**, 269–276 (1991).
44. Evans, R.L., Chess, L., Levine, H. & Schlossman, S.F. Antibody-dependent cellular cytotoxicity by allosensitized human T cells. *J. Exp. Med.* **147**, 605–610 (1978).
45. Velders, M.P. et al. The impact of antigen density and antibody affinity on antibody-dependent cellular cytotoxicity: relevance for immunotherapy of carcinomas. *Br. J. Cancer* **78**, 478–483 (1998).
46. Orcutt, K.D. et al. A modular IgG-scFv bispecific antibody topology. *Protein Eng. Des. Sel.* **23**, 221–228 (2010).
47. Klein, C., Schaefer, W. & Regula, J.T. The use of CrossMAb technology for the generation of bi- and multispecific antibodies. *mAbs* **8**, 1010–1020 (2016).
48. Lo, M. et al. Effector-attenuating substitutions that maintain antibody stability and reduce toxicity in mice. *J. Biol. Chem.* **292**, 3900–3908 (2017).
49. Dao, T. et al. Therapeutic bispecific T-cell engager antibody targeting the intracellular oncoprotein WT1. *Nat. Biotechnol.* **33**, 1079–1086 (2015).
50. Grakoui, A. et al. The immunological synapse: a molecular machine controlling T cell activation. *Science* **285**, 221–227 (1999).
51. Bunnell, S.C. et al. T cell receptor ligation induces the formation of dynamically regulated signaling assemblies. *J. Cell Biol.* **158**, 1263–1275 (2002).
52. Egerton, M., Fitzpatrick, D.R., Catling, A.D. & Kelso, A. Differential activation of T cell cytokine production by the extracellular signal-regulated kinase (ERK) signaling pathway. *Eur. J. Immunol.* **26**, 2279–2285 (1996).
53. Hu, S.L. et al. S1P promotes IL-6 expression in osteoblasts through the PI3K, MEK/ERK and NF-κB signaling pathways. *Int. J. Med. Sci.* **17**, 1207–1214 (2020).
54. Hogan, P.G. Calcium-NFAT transcriptional signalling in T cell activation and T cell exhaustion. *Cell Calcium* **63**, 66–69 (2017).
55. Faroudi, M. et al. Lytic versus stimulatory synapse in cytotoxic T lymphocyte/target cell interaction: manifestation of a dual activation threshold. *Proc. Natl. Acad. Sci. USA* **100**, 14145–14150 (2003).
56. Purbhoo, M.A., Irvine, D.J., Huppa, J.B. & Davis, M.M. T cell killing does not require the formation of a stable mature immunological synapse. *Nat. Immunol.* **5**, 524–530 (2004).
57. Haber, L. et al. Generation of T-cell-redirecting bispecific antibodies with differentiated profiles of cytokine release and biodistribution by CD3 affinity tuning. *Sci. Rep.* **11**, 14397 (2021).
58. Poussin, M. et al. Dichotomous impact of affinity on the function of T cell engaging bispecific antibodies. *J. Immunother. Cancer* **9**, e002444 (2021).
59. Shimabukuro-Vornhagen, A. et al. Cytokine release syndrome. *J. Immunother. Cancer* **6**, 56 (2018).
60. Teachey, D.T. et al. Identification of predictive biomarkers for cytokine release syndrome after chimeric antigen receptor T-cell therapy for acute lymphoblastic leukemia. *Cancer Discov.* **6**, 664–679 (2016).
61. Maude, S.L., Barrett, D., Teachey, D.T. & Grupp, S.A. Managing cytokine release syndrome associated with novel T cell-engaging therapies. *Cancer J.* **20**, 119–122 (2014).
62. Giavridis, T. et al. CAR T cell-induced cytokine release syndrome is mediated by macrophages and abated by IL-1 blockade. *Nat. Med.* **24**, 731–738 (2018).
63. Hettich, M., Lahoti, J., Prasad, S. & Niedermann, G. Checkpoint antibodies but not T cell-recruiting diabodies effectively synergize with TIL-inducing γ-irradiation. *Cancer Res.* **76**, 4673–4683 (2016).
64. Linsley, P.S. & Long, S.A. Enforcing the checkpoints: harnessing T-cell exhaustion for therapy of T1D. *Curr. Opin. Endocrinol. Diabetes Obes.* **26**, 213–218 (2019).
65. Döhner, H. et al. Diagnosis and management of AML in adults: 2022 recommendations from an international expert panel on behalf of the ELN. *Blood* **140**, 1345–1377 (2022).
66. Herrmann, M. et al. Bifunctional PD-1 × αCD3 × αCD33 fusion protein reverses adaptive immune escape in acute myeloid leukemia. *Blood* **132**, 2484–2494 (2018).
67. Wherry, E.J. & Kurachi, M. Molecular and cellular insights into T cell exhaustion. *Nat. Rev. Immunol.* **15**, 486–499 (2015).
68. Liu, Y.Y. et al. IL-2 regulates tumor-reactive $CD8^+$ T cell exhaustion by activating the aryl hydrocarbon receptor. *Nat. Immunol.* **22**, 358–369 (2021).
69. Singhaviranon, S., Dempsey, J.P., Hagymasi, A.T., Mandoiu, I.I. & Srivastava, P.K. Low-avidity T cells drive endogenous tumor immunity in mice and humans. *Nat. Immunol.* **26**, 240–251 (2025).
70. Nimmerjahn, F. & Ravetch, J.V. Antibody-mediated modulation of immune responses. *Immunol. Rev.* **236**, 265–275 (2010).
71. Carmichael, J.A. et al. The crystal structure of an anti-CEA scFv diabody assembled from T84.66 scFvs in V_L-to-V_H orientation: implications for diabody flexibility. *J. Mol. Biol.* **326**, 341–351 (2003).
72. Teplyakov, A., Obmolova, G., Luo, J.Q. & Gilliland, G.L. Crystal structure of B-cell co-receptor CD19 in complex with antibody B43 reveals an unexpected fold. *Proteins* **86**, 495–500 (2018).
73. Adair, J.R. et al. Humanization of the murine anti-human CD3 monoclonal anti-

body OKT3. *Hum. Antibodies Hybridomas* **5**, 41–47 (1994).
74. Zheng, S.Q. et al. MotionCor2: anisotropic correction of beam-induced motion for improved cryo-electron microscopy. *Nat. Methods* **14**, 331–332 (2017).
75. Rohou, A. & Grigorieff, N. CTFFIND4: fast and accurate defocus estimation from electron micrographs. *J. Struct. Biol.* **192**, 216–221 (2015).
76. Zivanov, J. et al. New tools for automated high-resolution cryo-EM structure determination in RELION-3. *Elife* **7**, e42166 (2018).
77. Pettersen, E.F. et al. UCSF Chimera—A visualization system for exploratory research and analysis. *J. Comput. Chem.* **25**, 1605–1612 (2004).
78. Emsley, P., Lohkamp, B., Scott, W.G. & Cowtan, K. Features and development of *Coot*. *Acta Crystallogr. D Biol. Crystallogr.* **66**, 486–501 (2010).
79. Adams, P.D. et al. *PHENIX*: a comprehensive Python-based system for macromolecular structure solution. *Acta Crystallogr. D Biol. Crystallogr.* **66**, 213–221 (2010).
80. Chen, V.B. et al. *MolProbity*: all-atom structure validation for macromolecular crystallography. *Acta Crystallogr. D Biol. Crystallogr.* **66**, 12–21 (2010).
81. Hovmöller, S., Zhou, T.P. & Ohlson, T. Conformations of amino acids in proteins. *Acta Crystallogr. D Biol. Crystallogr.* **58**, 768–776 (2002).

ADDITIONAL INFORMATION

Supplementary information The online version contains supplementary material available at https://doi.org/10.15302/vita.2026.03.0021.

Correspondence and requests for materials should be addressed to Zhiwei Huang.